



Surface modification of NiCo₂Te₄ nanoclusters: a highly efficient electrocatalyst for overall water-splitting in neutral solution

Leiming Tao^{a,b}, Min Huang^c, Shaojun Guo^d, Qinglong Wang^a, Man Li^a, Xin Xiao^a, Gengyu Cao^c, Yong Shao^e, Yan Shen^{a,*}, Yongqing Fu^f, Mingkui Wang^a

^a Wuhan National Laboratory for Optoelectronics, Huazhong University of Science and Technology, Luoyu Road 1037, Wuhan, 430074, PR China

^b School of Science, Guangdong University of Petrochemical Technology, Maoming, Guangdong, 525000, PR China

^c State Key Laboratory of Magnetic Resonance and Atomic and Molecular Physics, Wuhan Institute of Physics and Mathematics, Chinese Academy of Sciences, Wuhan, 430071, PR China

^d Department of Materials Science and Engineering, College of Engineering, Peking University, Beijing, 100871, PR China

^e Key Laboratory of the Ministry of Education for Advanced Catalysis Materials, Zhejiang Normal University, Jinhua, 321004, PR China

^f Faculty of Engineering and Environment, Northumbria University, Newcastle upon Tyne, NE1 8ST, UK

ARTICLE INFO

Keywords:

Nanocluster
NiCo₂Te₄
Water splitting
Electrocatalyst
Mixed-transition-metal

ABSTRACT

In this paper, we for the first time report the catalytic activity and durability of nickel cobaltite telluride (NiCo₂Te₄) nanocluster bifunctional catalysts can be significantly boosted by surface modification with perylene-tetracarboxylic-dianhydride for overall water-splitting in neutral solution. We reveal that tuning energy distribution of nanoclusters via a simple surface ligand can drastically increase the catalytic activity towards efficient hydrogen and oxygen evolution reaction simultaneously. A two-electrode based water electrolysis cell using this newly developed nanocluster catalyst operates at a low bias voltage of 1.55 V to achieve a current density of 10 mA·cm⁻² in near-neutral pH solution for overall water-splitting. This, to the best of our knowledge, represents the most efficient mixed-transition-metal-based electrode that has so far been reported for electrochemical water splitting.

1. Introduction

Electrochemical water-splitting is one of the most promising methods to efficiently produce hydrogen (and oxygen) for generating clean and renewable energy. Since the first observation of water electrolysis by van Trostwijk and Deiman in 1789, many different types of electrolysis cells have been proposed and constructed to produce hydrogen, mainly including alkaline electrolyzer, polymer electrolyte membrane electrolyzer (acidic), and solid oxide electrolyte [1]. Different electrolyzers function in slightly different ways, mainly due to the electrolyte materials and catalysts involved. Several metal oxides or metal phosphides routinely used for water splitting typically run at very high (alkaline) or low (proton exchange membrane) pH, which makes them prone to corrosion [2,3]. Consequently, there is a need to move away from the extreme pH regimes characteristic of such traditional commercial devices because such corrosive conditions limit the selection of electrodes and cell components [4]. Therefore, it remains a great challenge to develop efficient, durable, and low-cost new-generation catalysts for electrochemical water-splitting reaction in neutral

solution. Mixed-transition-metal (MTM)-based electrocatalysts have emerged as novel pH-universal electrocatalysts for water-splitting, owing to their desirable electrical conductivity, synergistic effect of bimetallic atoms, and structural stability [5,6]. The hydrogen evolution reaction (HER) activities of MTM-based electrocatalysts, e.g., Ni/Co-based phosphides/selenides/sulfides/oxides (Ni-Co-A, A = P, Se, S, O), are highly dependent on the adsorption strength of hydrogen to the anions (A). For example, Yu et al. suggested that P substitution of anions (A) in the Ni-Co-A could modulate the electron configuration, lower the hydrogen adsorption energy, and facilitate the desorption of hydrogen on the active sites, resulting in superior HER catalytic activity in alkaline solution [7]. In this case the transition metal tellurides (TMT) materials have attracted increasing interest for applications in electrochemical water splitting. The CoTe₂ possesses a low adsorption strength for H₂ and thus presents highly electro-catalytic activity toward the HER [8]. This works well with the NiTe₂ toward the HER, which shows a comparable activity (276 mV@10 mA·cm⁻²) to the CoTe₂ (246 mV@10 mA·cm⁻²) in acid solution [8,9]. These good performances are obtained in acidic solutions. It is noticed that there are

* Corresponding author.

E-mail address: ciac_sheny@mail.hust.edu.cn (Y. Shen).

<https://doi.org/10.1016/j.apcatb.2019.05.010>

Received 16 January 2019; Received in revised form 29 April 2019; Accepted 2 May 2019

Available online 03 May 2019

0926-3373/ © 2019 Elsevier B.V. All rights reserved.

few bifunctional catalytic materials exhibiting outstanding HER/OER activities in neutral-pH electrolytes. For example, very recently the Janus nickel cobalt phosphide catalysts have demonstrated remarkable activity and stability in neutral-pH water splitting [10].

Recently, nanometer-sized clusters (1–5 nm typically) have opened a doorway for new generation of highly efficient electrocatalysts with remarkable catalytic activity and selectivity [11,12]. For example, the bimetallic PtAu₂₄ nanoclusters have showed excellent electrochemically catalytic activity for H₂ production in acidic solution [11]. This can be attributed to their large surface/volume ratio and tunable electronic structure when the surface properties are the major concern for catalysts. In this regard, a large percentage of atoms are on or near the surfaces for clusters in such a small size regime. Particularly, the existence of vast interface between nanoclusters and the surrounding medium plays a profound effect. However, for practical application the long-term stability of nanocluster-based catalysts generally needs to be improved significantly [13]. Furthermore, the catalytic performance of clusters may become worse significantly as decreasing their size presumably due to slow transport of carriers. Therefore, various strategies including surface ligand engineering have been proposed to solve above-mentioned issues [10,14]. Indeed, some ligands can act as “poison”, limiting the accessibility of active sites as well as a “promoter”, resulting in an unpredicted activity and stability [15–17]. Currently, the surface ligands are only limited to small molecule ligands or graphene-molecule supporting layer systems. Therefore, it is urgent to develop new surface modifier with function of both ligand engineering and supporting layer for fine-tuning of nanocluster's properties.

This study, for the first time, reports a new type of electrocatalyst based on nickel cobaltite telluride (NiCo₂Te₄) nanoclusters for highly efficient water-splitting reaction in neutral solution. The NiCo₂Te₄ nanoclusters decorated with perylene-3,4,9,10-tetracarboxylic dianhydride (PTCDA) can be efficiently synthesized via an organic phase reaction process. The planar PTCDA molecule, consisting of a perylene core and two anhydrides, possesses high carrier mobility and excellent chemical stability [14]. The newly designed catalyst of NiCo₂Te₄/PTCDA exhibited an overpotential of 60 mV at 10 mA·cm⁻² and a turnover frequency of 20.9 s⁻¹ at a potential of -100 mV (vs. RHE) during the HER electrocatalytic activity in near-neutral pH solution. Additionally, this catalyst showed a high catalytic activity towards OER with a low overpotential of 120 mV at 10 mA·cm⁻². A current density of 10 mA·cm⁻² can be easily achieved at an applied cell voltage of 1.55 V across the neutral pH solution electrolyzer when this bifunctional electrocatalyst is applied as both the anode and cathode simultaneously.

2. Experimental section

Reagent clusters of Co(acac)₃ (1 mM), Ni(acac)₃ (0.5 mM), oleic acid (6 mM), oleylamine (6 mM), and benzyl ether (20 mL) were mixed and magnetically stirred inside a three-necked flask under a constant flow of nitrogen. The mixture was heated to 200 °C for 30 min and then 2 mL of TOP-Te (1 M) with 4 mL of oleic acid was quickly injected inside at 275 °C under the protection of nitrogen gas. The mixture was heated at 265 °C for another 10 min. The black-brown color mixture was cooled down to room temperature. Under ambient conditions, ethanol (40 mL) was added into the mixture. A black precipitate was obtained and followed by separation via centrifugation. The black product was dispersed into the hexane in the presence of oleic acid (0.05 mL) and oleylamine (0.05 mL). Centrifugation (10,000 rpm for 10 min) was applied to remove any undispersed residues in the solution. The product of NiCo₂Te₄ clusters was then precipitated, centrifuged (10,000 rpm, 10 min) to remove the solvent, and re-dispersed into hexane. Under identical conditions, reagents of Co(acac)₃ (1 mM) and Ni(acac)₂ (0.5 mM) with TOP-Se, TOP-S or TOP-O (where TOP = Trioctylphosphine) were processed to fabricate NiCo₂X₄

(X = Se, S, O) clusters that could be readily dispersed into hexane.

To synthesize NiCo₂Te₄/PTCDA, 40 mg of PTCDA was suspended in 20 mL of dichloromethane under a constant stirring at 30–35 °C, and then added into a 1 mL of 0.5 mM NiCo₂Te₄ clusters [14]. Ethanedioic acid was dissolved into the solution, which was stirred under the protection of nitrogen for 24 h. The volume of the solution was then reduced by one-half under a nitrogen gas flow, and the solution was filtered to remove any soluble materials. The filtrate was treated with charcoal and evaporated to obtain the final product of 110 mg. A pure sample was given using recrystallization from ether.

Density functional theory (DFT) calculations were performed using a Vienna Ab initio simulation package (VASP) simulation package [18]. The exchange and correlation functions with a Perdew-Burke-Ernzerh of generalized gradient corrected approximation (GGA) [19] and projector-augmented wave (PAW) [20] pseudopotentials were used during the calculations. The wave function was described with a plane wave basis set and an energy cutoff of 400 eV was used. The PTCDA films were modeled with a slab supercell containing two PTCDA molecules. NiCo₂Te₄ clusters were put onto the PTCDA molecules at the site where two PTCDA were connected in various orientations to search for the most stable structures. The vacuum thickness was set to be 10.0 Å which separated the slabs. A single Γ point was used in sampling the Brillouin zone due to the numerical limitations. For accurately analyzing the interactions between PTCDA molecules and NiCo₂Te₄ clusters as well as the inter-PTCDA interactions, the van der Waals interactions were corrected using the vdW-D2 method [21]. The effective values of U (U_{eff}) for Co and Ni were chosen to be 6.42 eV and 6.31 eV based on previous study [22,23].

3. Results and discussion

The NiCo₂Te₄ nanoclusters were firstly synthesized with high-temperature solution phase reaction according to previous reports [15]. The TEM characterization clearly illustrates that the obtained NiCo₂Te₄ clusters are about 1.98 nm in diameter with a narrow size distribution (Fig. 1A). The high-resolution TEM image in Fig. 1B reveals an interplanar spacing of 0.28 nm assigning to the (011) planes of NiCo₂Te₄ nanoclusters. Fig. 1C shows the XRD patterns of as-synthesized NiCo₂Te₄ nanoclusters (curve 1) which are perfectly agreed with a cubic structured spinel (space group, FD-3 m) with lattice constants of $a = b = c = 7.546$ Å and lattice angles of $\alpha = \beta = \gamma = 60.007^\circ$ (Figs. S1a and S1b). The diffraction peaks match with those of the CoNiTe₂ (curve 2, JCPDS card No. 03-065-3377) and NiTe₂ (curve 3, JCPDS card No. 03-065-3377). The energy-dispersive X-ray (EDX) spectrum characterization and the integrated atomic molar ratio further verify the composition of samples to be NiCo₂Te₄ (Fig. 1D). The elements of Ni, Co, and Te are uniquely distributed in the NiCo₂Te₄ nanoclusters (Figs. 1E–1H).

Fig. 2A outlines the synthesis procedures of NiCo₂Te₄/PTCDA nanoclusters through a ring opening reaction among NiCo₂Te₄ and planar PTCDA (Figs. S1c and S1d) mixture in dichloromethane at 30–35 °C [24–26]. The diffraction peaks in the XRD patterns of the as-synthesized NiCo₂Te₄/PTCDA (Fig. 2B) at $2\theta > 30^\circ$ can be well-assigned to the NiCo₂Te₄ while those less than 30° correspond to the planar structured PTCDA (Fig. S1e). The well-crystallized NiCo₂Te₄ nanoclusters are uniformly distributed onto the PTCDA platform (Fig. 2C and D). The binding NiCo₂Te₄ onto planar PTCDA was further experimentally verified by X-ray photoelectron spectroscopy (XPS) characterization. For the Te 3d spectrum of NiCo₂Te₄, the peaks at 572.3 eV and 582.6 eV correspond to Te²⁻ bonds of the Te 3d_{5/2} and Te 3d_{3/2}. For the XPS Te3d spectrum of NiCo₂Te₄/PTCDA, the newly appeared peaks at 576 eV and 586.4 eV are assigned to Te-O bonds (Fig. 2E). Fig. 2F shows the C 1s spectra of NiCo₂Te₄/PTCDA, NiCo₂Te₄, and PTCDA samples. The peaks at 288.8 eV and 290 eV are assigned to the O=C–O–C=O of cyclic anhydride from the PTCDA. There are seven main peaks, i.e., the peak at 771.4 eV for Co⁰, the peaks at 782.7 eV and 796.7 eV for Co²⁺, the peaks at 780.1 eV and 795 eV for Co³⁺, and two peak satellite at

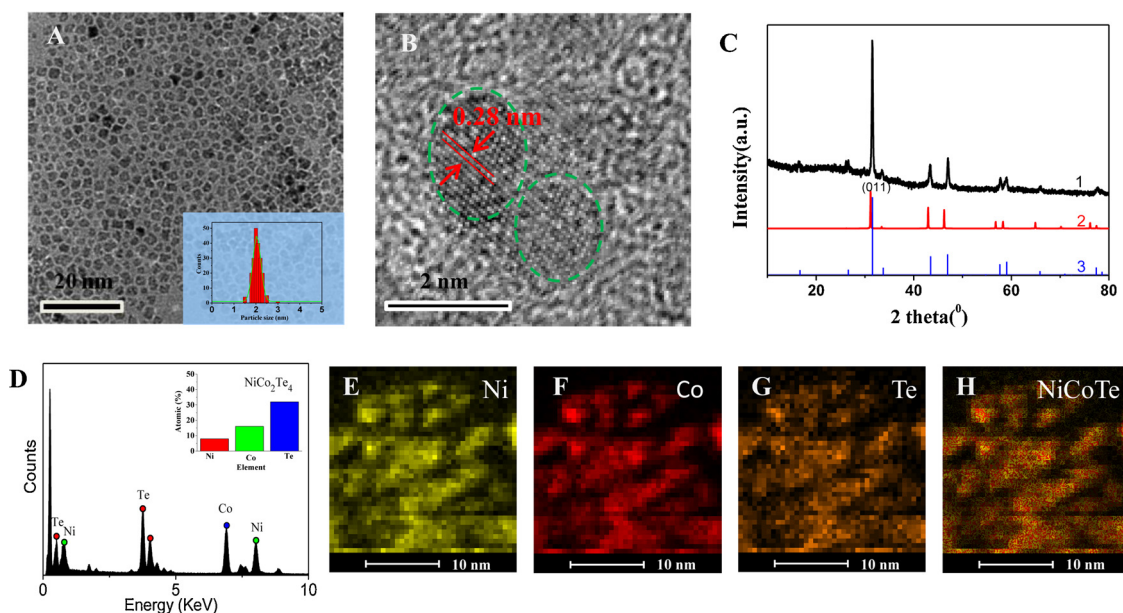


Fig. 1. (A) Transmission electron microscope (TEM) image, (B) HR-TEM, (C) X-ray diffraction patterns of as-synthesized-NiCo₂Te₄ (curve 1), CoNiTe₂ (curve 2), NiTe₂ (curve 3), (D) TEM-EDX spectrum of as-synthesized-NiCo₂Te₄. The inset shows the clusters integrated atomic molar ratio distribution. (E–G) EDX elemental mapping of Ni, Co, Te, and (H) the composed RGB image obtained by superposing the three elemental maps for the sample of NiCo₂Te₄.

788.5 eV and 804.2 eV in the NiCo₂Te₄ cluster, respectively (Fig. S3a). The intensity ratio of Co²⁺/Co³⁺ is about 0.7 for the NiCo₂Te₄ cluster sample. There are six main peaks, corresponding to the Co³⁺ (the peaks at 779.7 eV and 795.8 eV), Co²⁺ (the peaks at 782 eV and 798.3 eV), and two peak satellite at 785.5 eV and 802.4 eV in the NiCo₂Te₄/PTCDA composite (Fig. S3b). The intensity ratio of Co²⁺/Co³⁺ is about 1.1 for the NiCo₂Te₄/PTCDA composite. There are six main peaks for Ni in the NiCo₂Te₄ cluster, corresponding to the Ni²⁺ (at 854.4 eV and 872.4 eV), Ni³⁺ (at 856.0 eV and 874.0 eV), satellite peak at 861.1 eV and 879.1 eV, respectively (Fig. S3c). With regarding to the element of Ni, the binding energy values of Ni 2p XPS spectrum at 853.7 eV and 872.6 eV for the NiCo₂Te₄ cluster (Fig. S3c) and the NiCo₂Te₄/PTCDA (Fig. S3d) composite are assigned to the Ni 2p_{3/2} and Ni 2p_{1/2}, corresponding to a Ni²⁺ oxidation state. The peak at 880.6 eV corresponding to the O–Ni bond is almost at the same position for those of NiCo₂Te₄/PTCDA and NiCo₂Te₄. A possible mechanism for the chemical binding of PTCDA could be firstly correlated with the opening ring step of anhydride terminal groups (O=C–O–C=O) followed by a formation of C–O–Te bond between the Te atom of NiCo₂Te₄ and the oxygen (O_a) atom of PTCDA (Fig. S2).

We computed the charge density difference of NiCo₂Te₄ and NiCo₂Te₄/PTCDA (e.g., $\Delta\rho = \rho_1 - \rho_2 - \rho_{\text{PTCDA}}$) before and after surface modification to explore the effect of chemical binding between the NiCo₂Te₄ and PTCDA molecules, where the ρ_1 and ρ_2 represent the charge densities of NiCo₂Te₄ clusters modification with and without PTCDA molecules, respectively, and ρ_{PTCDA} is the charge density of PTCDA molecules. Figs. S4a–4c present the simulation result of charge-displacement. The analysis on the Bader's charge shows that a number of 0.7 *e* transfers from the NiCo₂Te₄ to PTCDA once combining both of them together. As shown in Table S2, the conduction band of PTCDA (–4.49 eV) is larger than the conduction band of NiCo₂Te₄ (–6.11 eV). The electron shall flow from NiCo₂Te₄, the one with higher Fermi level, to PTCDA, the one with lower Fermi level. In other words, in the composite of NiCo₂Te₄/PTCDA, the PTCDA possesses a higher charge density than the NiCo₂Te₄, which could induce a strong attraction between the NiCo₂Te₄ and PTCDA (possible through O_a–Te as discussed above). Our latest results, obtained using Fourier transform infrared spectroscopy characterization, also confirmed the interaction between the PTCDA and NiCo₂Te₄ (Fig. S4d).

Fig. 3A presents the linear sweep voltammetry (LSV) curves for the NiCo₂Te₄/PTCDA electrode to characterize their HER activity in 1 M phosphate buffer solution (PBS, pH = 7) recorded at a scan rate of 5 mV·s^{–1}. The NiCo₂Te₄/PTCDA achieved a current density of 10 and 100 mA·cm^{–2} at an applied potential of 60 and 120 mV (vs. RHE), respectively. Under the same condition, the NiCo₂Te₄ or PTCDA electrode showed less electrocatalytic activity to the HER. Fig. 3B presents electrochemical surface area (ECSA)-corrected Tafel plots derived from Koutecky-Levich plots for the NiCo₂Te₄/PTCDA and NiCo₂Te₄. A small Tafel slopes for the NiCo₂Te₄/PTCDA electrode (38 mV·dec^{–1}) indicates its efficient HER electrocatalytic performance. This result further suggests that the HER on the NiCo₂Te₄/PTCDA proceeds through Volmer-Tafel mechanism and the H + H recombination step is rate limiting [27]. The metric of catalysts was further evaluated in terms of turn over frequency (TOF) according to Equation 1 [28] and the results are presented in the inset of Fig. 3B.

$$\text{TOF} = \frac{J \times A}{z \times F \times m} \quad (1)$$

where *J* is the current density (A·cm^{–2}) at an overpotential of 0.1 V, *A* being the electrochemical active surface area (ECSA), *m* being the mass of active materials (in mole), *z* being the number of the transferred electrons (*z* = 2 for H₂ and *z* = 4 for O₂), respectively. Clearly, the NiCo₂Te₄/PTCDA electrode has the highest value of TOF at 27.1 s^{–1}, which is about 4 times larger than that of the NiCo₂Te₄ sample (6.5 s^{–1}). Fig. 2C compares the Tafel plots and overpotential at 10 mA·cm^{–2} for various reported HER catalysts, verifying the good performance of NiCo₂Te₄/PTCDA. The Faraday efficiency (FE) of the NiCo₂Te₄/PTCDA electrode is nearly 100% for the HER in 1 M PBS medium based on the gas chromatography characterization results (Fig. S5). Electrochemical impedance spectroscopy (EIS) measurement results further reveal that the NiCo₂Te₄/PTCDA electrode has a smaller polarization resistance than that of NiCo₂Te₄ (Fig. 3D). This indicates that the increased activity of NiCo₂Te₄/PTCDA can be probably attributed to the small charge transfer resistance. It also suggests the molecular PTCDA with large π -conjugation could enhance charge transport and catalytic kinetics of the NiCo₂Te₄ electrode. Fig. 3E presents that NiCo₂Te₄/PTCDA electrolyzer can retain a current density of 10 mA·cm^{–2} over 20 h of continuous operation without obvious degradation, while this current

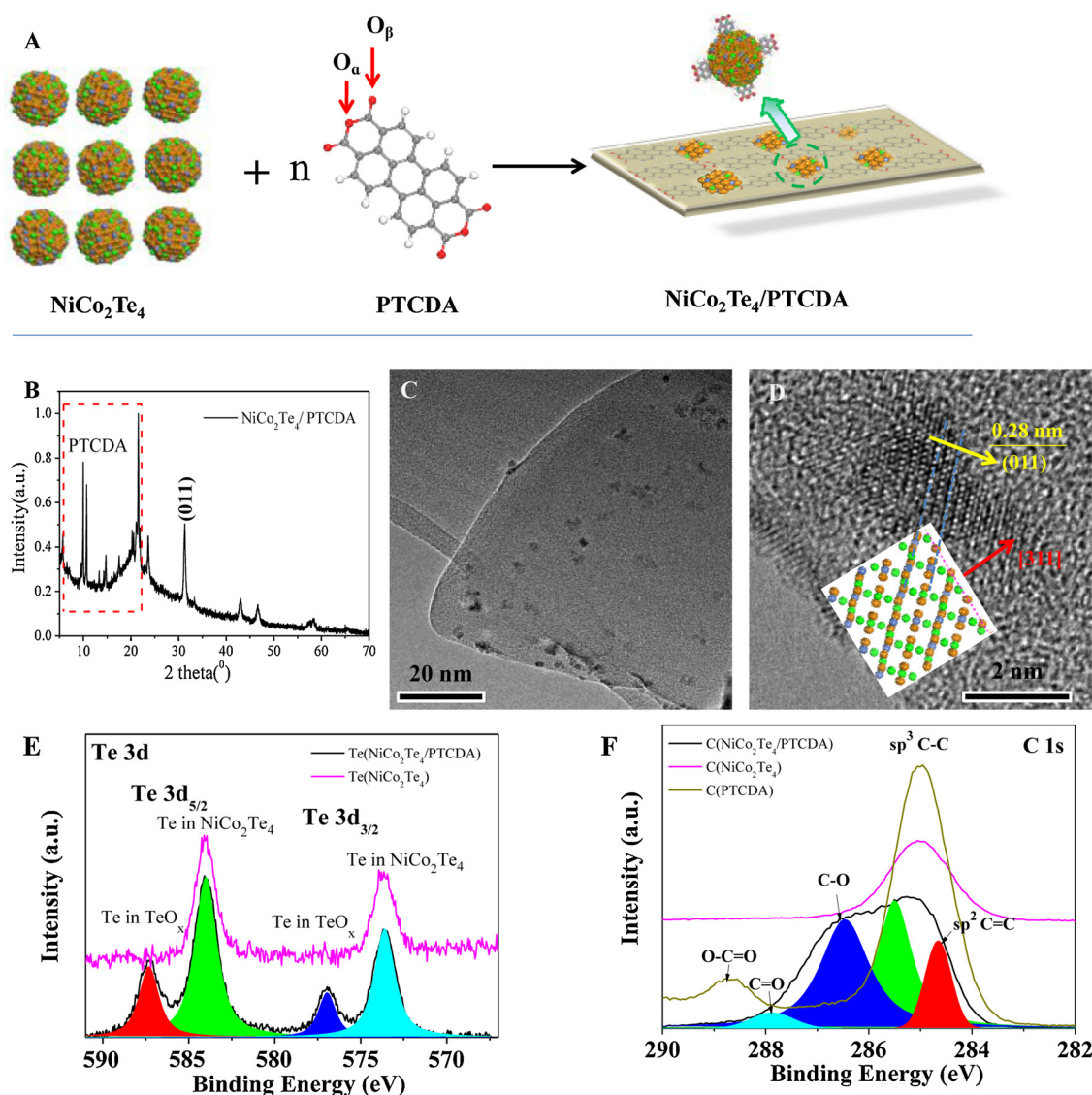


Fig. 2. (A) Schematic illustrations for synthesis of $\text{NiCo}_2\text{Te}_4/\text{PTCDA}$ (abbreviation of nickel cobaltite telluride clusters modified with perylene-3,4,9,10-tetracarboxylic dianhydride). The O_a and O_b represent O atoms at cyclic anhydride and carbonyl of PTCDA, respectively. (B) X-ray diffraction, (C) TEM images, and (D) HR-TEM of $\text{NiCo}_2\text{Te}_4/\text{PTCDA}$. The inset shows the model of NiCo_2Te_4 (011). (E) and (F) XPS spectra of Te 3d and C 1s for $\text{NiCo}_2\text{Te}_4/\text{PTCDA}$ and NiCo_2Te_4 samples.

density decreases in case of NiCo_2Te_4 . After tested with the continuous cyclic voltammetry characterization for 2000 cycles at a scanning rate of $10 \text{ mV} \cdot \text{s}^{-1}$, the $\text{NiCo}_2\text{Te}_4/\text{PTCDA}$ still exhibited a polarization curve with a stable overpotential of -60 mV at $10 \text{ mA} \cdot \text{cm}^{-2}$ (Fig. 3F).

Meanwhile, the $\text{NiCo}_2\text{Te}_4/\text{PTCDA}$ electrode also showed good catalytic behavior to the OER. In 1 M PBS the $\text{NiCo}_2\text{Te}_4/\text{PTCDA}$ achieved low overpotentials of 120 and 240 mV at current densities of 10 and $100 \text{ mA} \cdot \text{cm}^{-2}$ for the OER, with a Tafel slope of 50 mV per decade (Fig. 4A and B). The recorded overpotential for $\text{NiCo}_2\text{Te}_4/\text{PTCDA}$ was less than the NiCo_2O_4 electrode (150 mV at $10 \text{ mA} \cdot \text{cm}^{-2}$), however, the Tafel slope was higher than the NiCo_2O_4 electrode ($30 \text{ mV} \cdot \text{dec}^{-1}$ at $10 \text{ mA} \cdot \text{cm}^{-2}$). Fig. 4C compares the Tafel plots and overpotential at $10 \text{ mA} \cdot \text{cm}^{-2}$ for various reported OER catalysts, verifying the good performance of $\text{NiCo}_2\text{Te}_4/\text{PTCDA}$ for the OER. Fig. 4D presents that for the case of $\text{NiCo}_2\text{Te}_4/\text{PTCDA}$ electrode the current density retains over 20 h of continuous operation for OER without obvious degradation.

The catalysts were examined with XPS characterization after catalytic runs to investigate structural changes associated with the electrocatalysis. Fig. 4E presents the Te 3d XPS spectrum of the fresh $\text{NiCo}_2\text{Te}_4/\text{PTCDA}$ samples (curve 1) and that of after the HER testing (curve 2) and the OER testing (curve 3). For comparison purpose,

Fig. 4E shows the Te 3d of the NiCo_2Te_4 samples before and after the HER testing or the OER testing in curves 4–6, respectively. There are four main peaks, in which the peaks at 572.3 eV and 582.6 eV correspond to Te^{2-} bond, and the peaks at 576 eV and 586.4 eV are assigned to $\text{Te}-\text{O}_x$, respectively (Fig. 4E). For the Te 3d spectrum of NiCo_2Te_4 (curve 4), the peaks at 572.3 eV and 582.6 eV correspond to Te^{2-} bonds of the $\text{Te} 3d_{5/2}$ and $\text{Te} 3d_{3/2}$. For the XPS Te3d spectrum of $\text{NiCo}_2\text{Te}_4/\text{PTCDA}$ (curve 1), the newly appeared peaks at 576 eV and 586.4 eV are assigned to $\text{Te}-\text{O}$ bonds. Clearly, the Te 3d XPS spectrum kept almost identically for the $\text{NiCo}_2\text{Te}_4/\text{PTCDA}$ sample before and after electrochemical measurements. However, the Te3d signal for the NiCo_2Te_4 shows significant change after electrochemical testing by comparing the curve 4 to curves 5 and 6. This result demonstrates the function of the molecular PTCDA to protect Te from oxidation.

DFT calculation was carried out on the free energy for the possible adsorption of intermediates H^+ (O^*) on various positions within the $\text{NiCo}_2\text{Te}_4/\text{PTCDA}$ catalyst during the HER process. The DFT result in Fig. S6a verifies the effective contribution of ligands (i.e., PTCDA) to the adsorption of intermediates. In this case, the smallest value of adsorption energy for H^+ (O^*) on the obtuse angle position principally suggests the point for an easy desorption of intermediates. Furthermore,

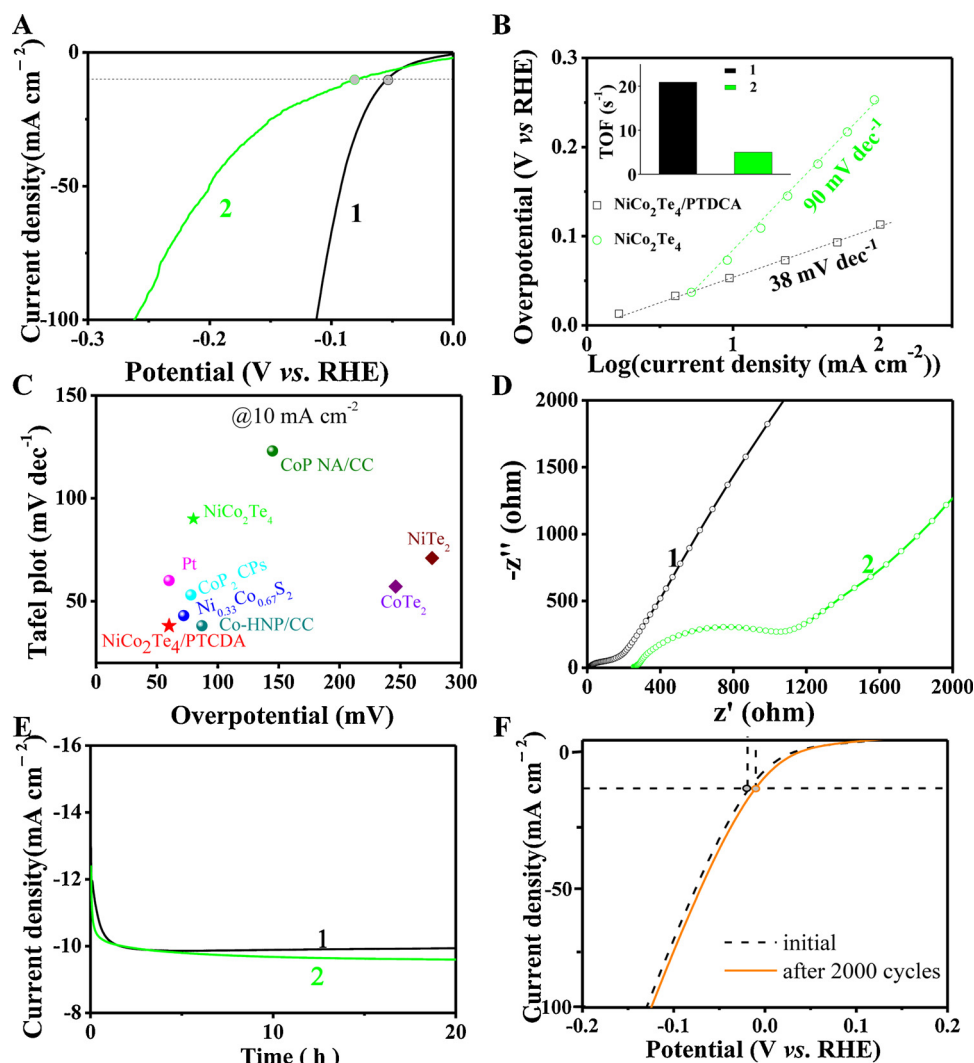


Fig. 3. (A) Linear sweep polarization curves obtained in 1 M PBS (pH = 7) for the NiCo₂Te₄/PTCDA (curve 1), NiCo₂Te₄ (curve 2). (B) The ECSA-corrected Tafel plots derived from Koutecky-Leviv plots. The inset shows ECSA corrected turnover frequency (TOF) of NiCo₂Te₄ and NiCo₂Te₄/PTCDA at a potential of -100 mV for HER in 1 M PBS. (C) The Tafel slope versus overpotential at 10 mA cm⁻² for various reported HER catalysts. Values were listed in Table S1. (D) Nyquist plots of NiCo₂Te₄/PTCDA (curve 1) and NiCo₂Te₄ (curve 2) from 10 kHz to 0.1 Hz at -0.2 V vs. RHE. (E) Chronoamperometric response recorded from NiCo₂Te₄/PTCDA (curve 1) and NiCo₂Te₄ (curve 2) at the constant overpotential to reach current density of -10 mA cm⁻² for HER. (F) The HER curves initial and after (curve 2) 2000 cycles with a scan rate of 100 mV s⁻¹ between 0.20 and -0.20 V. All electrochemical tests were conducted in 1 M PBS electrolyte.

we found the adsorption energies for these intermediates on the PTCDA at positions of obtuse angle and the terminal of PTCDA are lower than those of NiCo₂Te₄ (Fig. S6b). The adsorption of reaction intermediates onto the catalysts surface plays critical role on the bond-breaking and bond-forming during the catalytic processes. Frontier molecular orbital theory provides a good understanding of key steps involved in these surface catalytic reactions. The strength of adsorption and bonding of reactants on catalyst surfaces are closely linked to the symmetry and spin states of reactant's molecular or atomic orbitals, which are dependent on the matching between the energy levels of reactants and those of catalyst's surfaces and thus the content of electronic coupling between them. [29] For example, a chemical reaction can process easily when the electron Fermi energy equals that potential of the reactions in equilibrium. A good catalytic performance would be expected for the case with a high overlapping of the density of states (DOS) of catalysts with that of water molecules. Fig. 5A shows the calculated DOS profiles of NiCo₂Te₄/PTCDA, NiCo₂Te₄, Pt, PTCDA and H₂O molecules across the Fermi level with DFT simulation employing the Gerischer-Marcus model. [30] Clearly, the DOS patterns present an overlapping (indicated by a pink dotted circuit) between the oxidation and reduction potentials of the water molecules and that of Pt serving as an efficient catalyst toward electrochemical hydrogen production. Though the individual NiCo₂Te₄ (red line) or PTCDA (green line) has less electron distribution in this range, the energy levels of valence band and conduction band of NiCo₂Te₄ are shifted by modifying with PTCDA toward the levels of H₂O/O₂ and H₂/H₂O equivalent electrochemical

potentials, respectively. This indicates surface engineering of NiCo₂Te₄ with PTCDA can significantly tune the composites' energy levels.

We further synthesized several nanocluster-based catalysts including NiO, Co₃O₄, NiCo₂O₄, NiCo₂S₄, and NiCo₂Se₄ through controlling particle size but without surface modification with PTCDA and systematically evaluated their catalytic behaviors [30,31]. Fig. 5B illustrates the band diagram of Pt, NiCo₂Te₄/PTCDA, NiCo₂Te₄, NiCo₂Se₄, NiCo₂S₄, NiCo₂O₄, Co₃O₄, NiO, and PTCDA. The valence band positions of NiO (2.71 V) [32], Co₃O₄ (2.61 V) [33], NiCo₂O₄ (2.34 V) [34], NiCo₂S₄ (2.17 V) [35], NiCo₂Se₄ (1.77 V) and NiCo₂Te₄ (1.61 V) are approaching the potential of water-splitting. The NiCo₂Te₄ possesses a valence band position near to the potential of water-splitting among NiCo₂X₄ (X=O, S, Se, Te) (Table S2). After modifying with PTCDA, its (NiCo₂Te₄/PTCDA) valence band position (1.18 V) and conduction band position (-0.02 V) were further tuned toward the levels of H₂O/O₂ and H₂/H₂O couples, respectively (Fig. 5B).

For reactions with more than one possible product the presence of a surface can completely change the selectivity. The adsorption of reaction intermediates onto the catalysts surface plays critical role on the bond-breaking and bond-forming during the catalytic processes [36–40]. It is well-known that the HER process in alkaline medium is determined by the dissociation of water molecules, where two intermediate species forms, i.e., O⁻ and H⁺ which need to adsorb and desorb on catalyst surface with variable deriving energies to complete the reaction. In the particular case of hydrogen evolution, it turns out that these general principles can be quantified by analysing the free

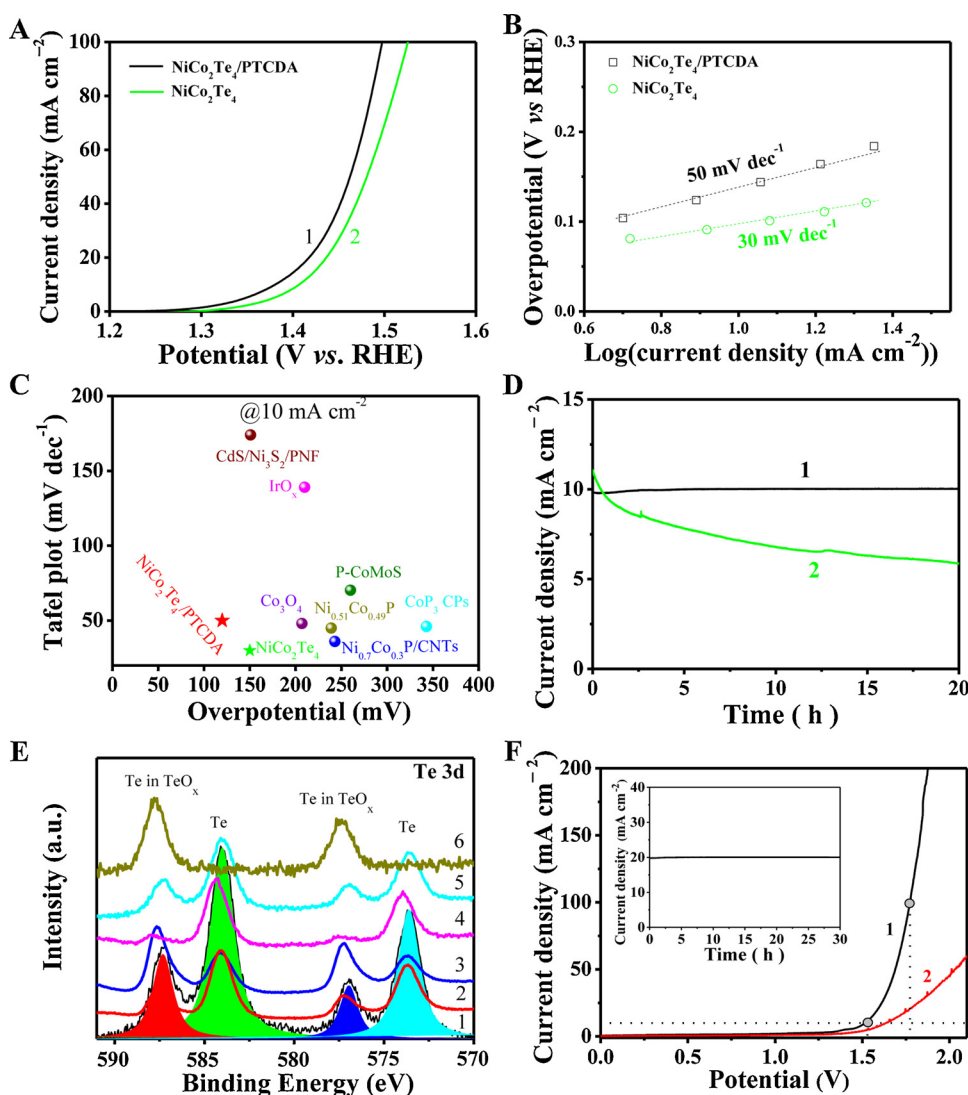


Fig. 4. (A) Linear sweep polarization curves for the $\text{NiCo}_2\text{Te}_4/\text{PTCDA}$. (B) The ECSA-corrected Tafel plots derived from Koutecky-Levich plots. (C) Tafel slope versus overpotential at 10 mA cm^{-2} for various reported OER catalysts. Values were listed in Table S1. (D) Chronoamperometric response recorded from the $\text{NiCo}_2\text{Te}_4/\text{PTCDA}$ (curve 1) and NiCo_2Te_4 (curve 2) at the constant overpotential to reach current density of 10 mA cm^{-2} for OER. (E) XPS spectra of Te 3d for the fresh $\text{NiCo}_2\text{Te}_4/\text{PTCDA}$ electrode (curve 1), after HER testing (curve 2), after the OER testing (curve 3), the fresh NiCo_2Te_4 electrode (curve 4), after the HER testing (curve 5), after the OER testing (curve 6). (F) Electrolyzer properties of $\text{NiCo}_2\text{Te}_4/\text{PTCDA}||\text{NiCo}_2\text{Te}_4/\text{PTCDA}$ (curve 1). The inset shows the chronoamperometric curve of the $\text{NiCo}_2\text{Te}_4/\text{PTCDA}||\text{NiCo}_2\text{Te}_4/\text{PTCDA}$ electrolyzer at a static potential of 1.61 V for 30 h. All electrochemical tests were conducted in 1 M PBS electrolyte.

energy of hydrogen adsorption ΔG_{H} . This quantity is a reasonable descriptor of hydrogen evolution activity for a wide variety of metals and alloys. Tuning of the spatial and energy distribution of valence electrons at the catalyst surface can thus be used to directly affect catalytic properties such as the activation energy barrier, which determines the reactivity and the selection of reaction pathways, and thus product selectivity. In principle, frontier molecular orbital theory indicates that the strength of the adsorption and bonding of reactants on catalyst surfaces is closely related to the symmetry and spin state of reactant molecular or atomic orbitals, and depends on matching the energy levels of the reactants to those of the catalyst surface as well. A good catalytic performance would be expected for the case with a high overlapping of the density of states (DOS) of catalysts with that of water molecules. Clearly, the DOS patterns present an overlapping (indicated by a pink dotted circuit) between the oxidation and reduction potentials of the water molecules and that of Pt serving as an efficient catalyst toward electrochemical hydrogen production. Though the individual NiCo_2Te_4 (red line) or PTCDA (green line) has less electron distribution in this range, the energy levels of valence band and conduction band of NiCo_2Te_4 are shifted by modifying with PTCDA toward the levels of $\text{H}_2\text{O}/\text{O}_2$ and $\text{H}_2/\text{H}_2\text{O}$ equilibrium electrochemical potentials, respectively.

Fig. 6A compares the adsorption free energy (ΔG_{H}) for hydrogen on these samples. The PTCDA has a larger ΔG_{H} value ($\sim 6.5 \text{ eV}$) than others, mainly due to the anhydride terminal groups ($\text{O}=\text{C}-\text{O}-\text{C}=\text{O}$) and its

weak 2D planar π -conjugation structure. As mentioned earlier, a strong ionic interaction (O_a-Te) between the NiCo_2Te_4 and PTCDA would decrease electronegativity of the NiCo_2Te_4 and reduce the ΔG_{H} between the NiCo_2Te_4 and PTCDA, respectively. Therefore, atomic hydrogen can be easily released from the $\text{NiCo}_2\text{Te}_4/\text{PTCDA}$ surface compared to others (Fig. 6A), which significantly enhances their catalytic activities during water-splitting [41]. Fig. 6B and Table S1 summarize the overpotentials (the error range being about 2 mV) of these samples ($\text{NiCo}_2\text{Te}_4/\text{PTCDA}$, NiCo_2O_4 , NiCo_2S_4 , NiCo_2Se_4 , NiCo_2Te_4 , NiO , Co_3O_4 and Pt) at 10, 20, and 100 mA cm^{-2} for the HER and the OER in 1 M PBS solution. Interestingly, all the compounds containing Co showed better HER performance than those of Ni-based counterparts. The integration of Ni and Co into the MTM electrocatalysts further improves their catalytic performance. This further verifies the MTM-based materials emerging as efficient electrocatalysts for water splitting [5,6]. The NiCo_2O_4 , NiCo_2S_4 , NiCo_2Se_4 and NiCo_2Te_4 have overpotentials of 330, 214, 142, and 80 mV at a current density of 10 mA cm^{-2} for the HER (Table S1), respectively. This behavior follows the electronegativity of the elements of O (3.44), S (2.58), Se (2.55), and Te (2.1) in the NiCo_2 -based compounds.

We further fabricated two-electrode ($\text{NiCo}_2\text{Te}_4/\text{PTCDA}||\text{NiCo}_2\text{Te}_4/\text{PTCDA}$) electrolysis cells using Nafion membrane as separator for efficient overall water-splitting. The $\text{NiCo}_2\text{Te}_4/\text{PTCDA}$ cell merely required bias voltages of 1.55, 1.61, and 1.78 V to reach current densities of 10, 20, and 100 mA cm^{-2} in the PBS solution (pH = 7) (Fig. 4F). A

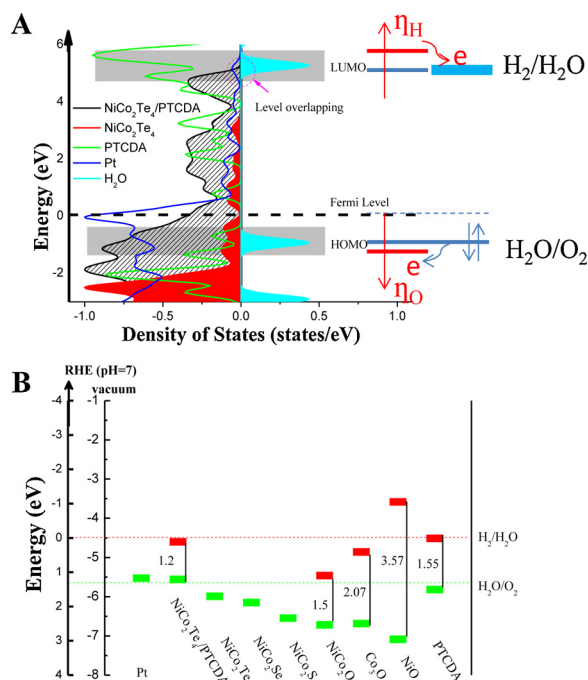


Fig. 5. (A) The calculated density of states (DOS) of NiCo₂Te₄/PTCDA (black), NiCo₂Te₄ (red), PTCDA (green), Pt (blue), and H₂O (cyan); (B) Bandgap energy, Valence band and Conduction band positions of several samples on an energy scale (eV) vs. RHE/Vacuum level (For interpretation of the references to colour in this figure legend, the reader is referred to the web version of this article).

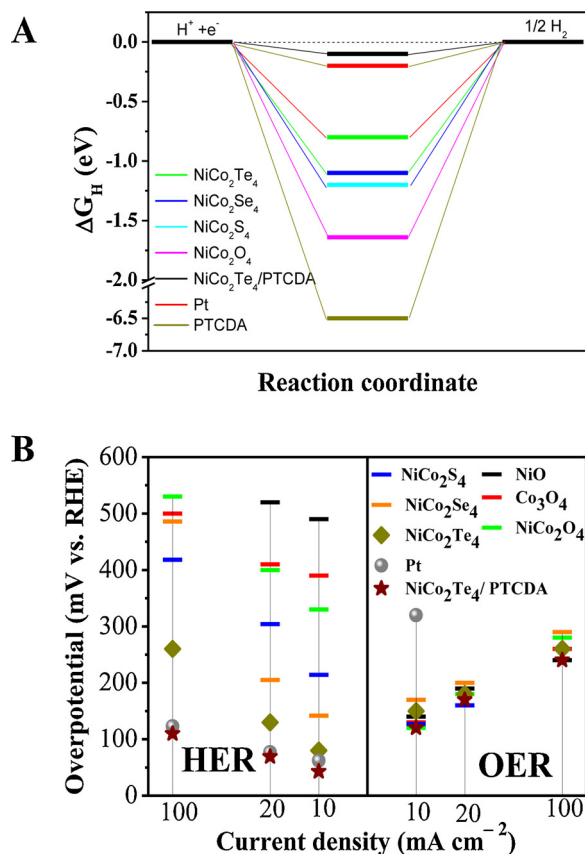


Fig. 6. (A) Hydrogen adsorption free energy ΔG_H diagrams; (B) Performance of catalysts (2 nm clusters of NiO, Co₃O₄, NiCo₂O₄, NiCo₂S₄, NiCo₂Se₄, NiCo₂Te₄, NiCo₂Te₄/PTCDA, and Pt) for HER and OER. The overpotentials obtained at 10, 20, and 100 mA cm⁻² on various catalysts in 1 M PBS.

current density of 10 mA cm⁻² can be obtained at a cell voltage of 1.55 V, representing an overpotential of 220 mV for overall water-splitting. The overpotential value is superior to most of previously reported electrocatalysts (Table S3), including the noble metal-based Pt/C||RuO₂ cell (green, 380 mV at 10 mA cm⁻²), FeB₂ (340 mV at 10 mA cm⁻²) [42], CoP (390 mV at 10 mA cm⁻²) [43], Co₃Se₄ (360 mV at 10 mA cm⁻²) [44]. The inset of Fig. 4F shows the stability of water splitting by the electrolysis cells (NiCo₂Te₄/PTCDA)||NiCo₂Te₄/PTCDA at a voltage of 1.61 V, producing gas bubbles of hydrogen and oxygen based on the gas chromatography characterization results (fig. S4). The NiCo₂Te₄/PTCDA cells exhibited an excellent stability for 30 h of long-term water electrolysis without obvious degradation when tested at a constant potential of 1.61 V (Fig. 4F and the inset).

4. Conclusion

In summary, this work presents the nanocluster catalysts for efficient overall water-splitting application. The newly designed catalyst of NiCo₂Te₄/PTCDA exhibited an overpotential of 60 mV at 10 mA cm⁻² and a turnover frequency of 20.9 s⁻¹ during the HER electrocatalytic activity in near-neutral pH solution. Additionally, this catalyst showed a high catalytic activity towards OER with a low overpotential of 120 mV at 10 mA cm⁻². A two-electrode water electrolysis cell using the NiCo₂Te₄/PTCDA only needed a low bias voltage of 1.55 V to acquire a current density of 10 mA cm⁻² for overall water-splitting. This is remarkably superior to those reported electrochemical activities of the transition metal catalysts. The excellent electrocatalytic activities of NiCo₂Te₄/PTCDA could be attributed to the enhanced charge transport, antioxidant properties and the perfect tuning of the energy distributions of valence electrons of NiCo₂Te₄ induced by surface ligand PTCDA.

Acknowledgments

The authors gratefully acknowledge financial support from the NSFC Major International (Regional) Joint Research Project NSFC-SNSF (51661135023), NSFC (21673091), the Fundamental Research Funds for the Central Universities (HUST: 2016YXMS031, 2018KFYXKJC034), the Director Fund of the WNLO, and the Open Funds of the State Key Laboratory of Electroanalytical Chemistry (SKLEAC201607), UK Engineering and Physical Sciences Research Council (EPSRC)EP/P018998/1, a Newton Mobility Grant (IE161019) from the UK Royal Society and the National Natural Science Foundation of China, and Royal Academy of Engineering UK-Research Exchange with China and India.

Appendix A. Supplementary data

Supplementary material related to this article can be found, in the online version, at doi:<https://doi.org/10.1016/j.apcatb.2019.05.010>.

References

- [1] Q. Xu, H. Jiang, H. Zhang, Y. Hu, C. Li, Appl. Catal. B 242 (2019) 60–66.
- [2] Y. Ma, C. Wu, X. Feng, H. Tan, L. Yan, Y. Liu, Z. Kang, E. Wang, Y. Li, Energy Environ. Sci. 10 (2017) 788–798.
- [3] S. Dutta, A. Indra, Y. Feng, H. Han, T. Song, Appl. Catal. B 241 (2019) 521–527.
- [4] Z. Kou, L. Zhang, Y. Ma, X. Liu, W. Zang, J. Zhang, S. Huang, Y. Du, A.K. Cheetham, J. Wang, Appl. Catal. B 243 (2019) 678–685.
- [5] R. Zhang, X. Wang, S. Yu, T. Wen, X. Zhu, F. Yang, X. Sun, X. Wang, W. Hu, Adv. Mater. 29 (2017) 1605502.
- [6] T. Tang, W. Jiang, S. Niu, N. Liu, H. Luo, Y. Chen, S. Jin, F. Gao, L. Wan, J. Hu, J. Am. Chem. Soc. 139 (2017) 8320–8328.
- [7] Z. Fang, L. Peng, Y. Qian, X. Zhang, Y. Xie, J.J. Cha, G. Yu, J. Am. Chem. Soc. 140 (2018) 5241–5247.
- [8] T. Lu, C. Chen, M. Basu, C. Ma, R. Liu, Chem. Commun. 51 (2015) 17012–17015.
- [9] K. Wang, Z. Ye, C. Liu, D. Xi, C. Zhou, S. Shi, H. Xia, G. Liu, G. Qiao, ACS Appl. Mater. Interfaces 8 (2016) 2910–2916.
- [10] R. Wu, B. Xiao, Q. Gao, Y. Zheng, X. Zheng, J. Zhu, M. Gao, S. Yu, Angew. Chem., Int. Ed. 130 (2018) 15671–15675.
- [11] Y. Ge, S. Gao, P. Dong, R. Baines, P.M. Ajayan, M. Ye, J. Shen, Nanoscale 9 (2017)

- 5538–5544.
- [12] K. Kwak, W. Choi, Q. Tang, M. Kim, Y. Lee, D. Jiang, D. Lee, *Nat. Commun.* 8 (2017) 14723.
- [13] J. Xu, T. Liu, J. Li, B. Li, Y. Liu, B. Zhang, D. Xiong, I. Amorim, W. Li, L. Liu, *Energy Environ. Sci.* 11 (2018) 1819–1827.
- [14] K. Li, Y. Li, Y. Wang, J. Ge, C. Liu, W. Xing, *Energy Environ. Sci.* 11 (2018) 1232–1239.
- [15] L. Cao, Y. Wang, T. Chen, W. Zhang, X. Yu, K. Ibrahim, J. Wang, H. Qian, F. Xu, D. Qi, A.T. Wee, *J. Chem. Phys.* 135 (2011) 174701.
- [16] J. Edman, H. Simmons, *J. Org. Chem.* 33 (1968) 3808–3816.
- [17] Y. Zou, L. Kilian, A. Schöll, T. Schmidt, R. Fink, E. Umbach, *Surf. Sci.* 600 (2006) 1240–1251.
- [18] G. Kresse, J. Furthmüller, *Phys. Rev. B* 54 (1996) 11169–11186.
- [19] J. Perdew, K. Burke, M. Ernzerhof, *Phys. Rev. Lett.* 77 (1996) 3865–3868.
- [20] G. Kresse, D. Joubert, *Phys. Rev. B* 59 (1999) 1758–1775.
- [21] S. Grimme, *J. Comput. Chem.* 27 (2006) 1787–1799.
- [22] J. He, S. Ma, P. Zhou, C. Zhang, C. He, L. Sun, *J. Phys. Chem. C* 116 (2012) 26313–26321.
- [23] J. He, P. Zhou, N. Jiao, S. Ma, K. Zhang, R. Wang, L. Sun, *Sci. Rep.* 4 (2014) 4014.
- [24] J. Edman, H. Simmons, *J. Org. Chem.* 33 (1968) 3808–3816.
- [25] Y. Zou, L. Kilian, A. Scholl, T. Schmidt, R. Fink, E. Umbach, *Surf. Sci.* 600 (2006) 1240–1251.
- [26] G. Gavrila, D. Zahn, W. Braun, *Appl. Phys. Lett.* 89 (2006) 162102.
- [27] B. Conway, B. Tilak, *Electrochim. Acta* 47 (2002) 3571–3594.
- [28] M. Gong, Y. Li, H. Wang, Y. Liang, J. Wu, J. Zhou, J. Wang, T. Regier, F. Wei, H. Dai, *J. Am. Chem. Soc.* 135 (2013) 8452–8455.
- [29] A. Bard, L. Faulkner, *Electrochemical methods: fundamentals and applications*, 2nd edn, *J. Chem. Educ.* 60 (2001) 80–89.
- [30] M. Greiner, M. Helander, W. Tang, Z. Wang, J. Qiu, Z. Lu, *Nat. Mater.* 11 (2011) 76.
- [31] C. Chuang, P. Brown, V. Bulović, M. Bawendi, *Nat. Mater.* 13 (2014) 796.
- [32] Y. Maseki, H. Kato, A. Kudo, *Energy Environ. Sci.* 2 (2009) 306.
- [33] H. Zhang, S. Pokhrel, Z. Ji, H. Meng, X. Wang, S. Lin, C. Chang, L. Li, R. Li, B. Sun, M. Wang, Y. Liao, R. Liu, T. Xia, L. Mädler, A. Nel, *J. Am. Chem. Soc.* 136 (2014) 6406–6420.
- [34] K. Dileep, B. Loukya, P. Silwal, A. Gupta, R. Datta, *J. Phys. D Appl. Phys.* 47 (2014) 405001.
- [35] C. Xia, P. Li, A.N. Gandhi, U. Schwingenschlögl, H. Alshareef, *Chem. Mater.* 27 (2015) 6482–6485.
- [36] J. Nørskov, T. Bligaard, A. Logadottir, J.R. Kitchin, J. Chen, S. Pandalov, U. Stimming, *J. Electrochem. Soc.* 152 (2005) J23–J26.
- [37] J. Rossmeisl, A. Logadottir, J. Nørskov, *Chem. Phys.* 319 (2005) 178–184.
- [38] J. Greeley, T. Jaramillo, J. Bonde, I. Chorkendorff, J. Nørskov, *Materials for Sustainable Energy* (2011) 280–284.
- [39] J. Rossmeisl, Z. Qu, H. Zhu, G. Kroes, J. Nørskov, *J. Electroanal. Chem. Lausanne (Lausanne)* 607 (2007) 83–89.
- [40] I. Man, H. Su, F. Calle-Vallejo, H. Hansen, J. Martínez, N. Inoglu, J. Kitchin, T. Jaramillo, J. Nørskov, J. Rossmeisl, *ChemCatChem* 3 (2011) 1159–1165.
- [41] E. Yoo, T. Okata, T. Akita, M. Kohyama, J. Nakamura, I. Honma, *Nano Lett.* 9 (2009) 2255–2259.
- [42] H. Li, P. Wen, Q. Li, C. Dun, J. Xing, C. Lu, S. Adhikari, L. Jiang, D. Carroll, S. Geyer, *Adv. Energy Mater.* 7 (2017) 1700513.
- [43] Y. Zhu, Y. Liu, T. Ren, Z. Yuan, *Adv. Funct. Mater.* 25 (2015) 7337–7347.
- [44] W. Li, X.F. Gao, D. Xiong, F. Wei, W. Song, J. Xu, L. Liu, *Adv. Energy Mater.* 7 (2017) 1602579.